JOURNAL OF PROPULSION AND POWER
Vol. 23, No. 2, March–April 2007

Near-Blowoff Dynamics of a Bluff-Body Stabilized Flame

Suraj Nair*
Woodward Industrial Controls, Fort Collins, Colorado 80525
and
Tim Lieuwen†
Georgia Institute of Technology, Atlanta, Georgia 30332-0150

DOI: 10.2514/1.24650

This paper describes an experimental investigation of the dynamics of a near-blowoff, bluff-body stabilized flame. This work is motivated by a number of prior observations showing that near-blowoff flames exhibit enhanced unsteadiness. Laser sheet imaging studies and particle image velocimetry velocity field measurements show that the transient dynamics of these flames occur in two distinct stages before blowoff. The first stage is manifested by the presence of localized "holes" in the flame sheet, at locations where the instantaneous stretch rate exceeds the extinction stretch rate. During this stage, the overall flame and wake dynamics appear essentially unaltered and, moreover, the flame can persist indefinitely, although with enhanced unsteadiness. As the equivalence ratio is further decreased, the size of the flame region affected and the duration of these events increases monotonically. As the blowoff point is approached further, this leads to the second stage, large-scale alterations of the wake dynamics, violent flapping of the flame front, and even larger straining of the flame. In some cases, the flow in this second stage bears striking resemblance to the asymmetric von Kármán type flowfield.

I. Introduction

FLAMES can only be stabilized in high-velocity reactant streams over a certain range of conditions. As such, determining these conditions, and those for which the flame cannot be stabilized (referred to here as blowout), is an important issue in any practical combustion device; for example, it is a concern in aircraft engines during sudden changes in throttle setting. During rapid decelerations, the fuel flow rate can be reduced very quickly, whereas the slower air flow transient rate is controlled by the rotational inertia of the compressor [1]. In addition, stability limits are narrowed at high-altitude conditions, making blowout a concern in certain flight regimes for aircraft engine main burners or augmenters.

Blowout is also an issue in land-based industrial systems, for which the engines are required to operate reliably over long periods with minimal shutdown time [2]. Stringent emissions requirements have motivated these engines to operate premixed and fuel lean [3], in order to minimize combustion temperatures and, therefore, NO_x. Such lean operation necessarily requires operating in the vicinity of the blowout point. If it occurs, blowout requires a system shutdown and restart, which increases maintenance costs and reduces part life and availability.

Although a variety of approaches are used to stabilize flames, bluff-body stabilization is of particular interest here. Bluff bodies are used for flame stabilization in a variety of propulsion and industrial combustion systems. They are employed for supplementary firing in industrial boilers and heat recovery steam generators and are also used in ramjet and turbojet afterburner systems. In addition, they are often used in fundamental studies of turbulent flame characteristics [4] or as computational test cases [5,6] and have been targeted as one of three stationary laboratory premixed flame configurations for study by the International Workshop on Premixed Flames participants [7].

An extensive literature on the time-average characteristics of such flames exists, such as contained in Vols. 3–5 in the *Proceedings of the Combustion Institute* by Scurlock [8], Shipman [9], Longwell [10], Zukoski [11], and others. These studies particularly focused upon the processes responsible for flame stabilization and the development of physics-based correlations of flame stability limits. For example, according to Zukoski [12], ignition of the incoming fresh, unburned mixture occurs in the shear layer, where it mixes with combustion products from the recirculation zone behind the bluff body. The reacting mixture flows downstream through the shear layer and ignites the neighboring mixture kernels. When it reaches the end of the wake, it is entrained into the recirculating flow, which conveys it upstream to mix with and ignite the shear layer. The flame remains anchored as long as this feedback process continues. He defines a "critical ignition delay time" that must be less than the time of contact between the incoming reactants and hot wake:

$$t_{BO.} = L_r/U_{BO} \tag{1}$$

where L_r is the recirculation zone length and U_{BO} is the flow velocity. However, due to poor understanding of the recirculation zone entrainment dynamics by vortex shedding and turbulent mixing processes, rational correlations of this very important length scale were never developed in a satisfactory manner.

The dynamic characteristics of the flame and flowfield have received significantly less attention and are less well understood. For example, it is well known that the flowfield is substantially altered between the reacting and nonreacting situations, largely due to qualitative differences in the shear layer dynamics. Although vortex dynamics have been extensively investigated in nonreacting flows [13], a number of unanswered questions remain in the reacting flow case; for example, the very fundamental question of whether and when vortex shedding occurs in the reacting case is uncertain [14].

This study is particularly interested in the dynamics of near-blowoff flames. This work is motivated by observations that flames near blowoff exhibit a variety of transient characteristics, as detailed by the authors for bluff body, pilot, and swirl stabilized flames [15,16]. In the specific context of bluff-body flames, this observation was apparently first made by Nicholson and Field [17], who described large-scale pulsations in the bluff-body flame as it was blowing off. In addition, Hertzberg et al. [14] found evidence of vortex shedding in these flames near blowoff, as manifested by the occurrence of discrete peaks in the velocity spectra. Although not treating blowoff explicitly, Soteriou and Mehta [18] and Erickson

Received 16 April 2006; revision received 28 July 2006; accepted for publication 28 July 2006.

*Mechanical Engineer/Analyst, 1000 East Drake Road.
†Associate Professor, 270 Ferst Drive; tim.lieuwen@aerospace.gatech.edu. Senior Member AIAA.

et al. [19] considered the factors responsible for the transition from the asymmetric von Kármán vortex shedding mode in the nonreacting case to the shear layer dominated vorticity often observed in the reacting case. They show that this transition phenomenon is highly dependent upon the dilatation ratio across the flame; in particular, that the von Kármán vortex shedding mode does occur for low dilatation ratios ($T_b/T_u < 1.5$–2) flames, and is suppressed at higher dilatation ratios.

The objective of this work is to characterize the dynamics of near-blowoff flames in order to better understand these unsteady processes and also to aid in "smarter" signal processing schemes to detect and predict blowoff. We next proceed to a discussion of the experimental apparatus, flow diagnostics, and results.

II. Experimental Facility and Instrumentation

Experiments were carried out with a 9.5 mm cylindrical bluff body, mounted at the immediate exit of a square section channel ($92 \times 92 \times 914$ mm) to stabilize the flame, shown in Fig. 1. Natural gas and air are mixed in a plenum chamber. It then passes through a flashback arrestor, a series of settling screens and flow straighteners, and finally exhausts into the ambient environment at the burner exit. All measurements were made at atmospheric conditions.

Particle image velocimetry (PIV) was employed to obtain instantaneous whole flowfield measurements [20]. Because of its relatively low sampling rate, they could not be used to visualize the temporal dynamics of the flame through an extinction event, but were quite useful for providing snapshots of the flowfield. The air is seeded with 2–3 μm aluminum oxide particles, which were illuminated using a laser light sheet produced from the second harmonic output (532 nm) of a dual-head, pulsed Nd:YAG laser. Each laser head provides 150 mJ/pulse at 10 Hz. The beam is converted into a 2-mm-thin sheet with two cylindrical lenses and passes through the midpoint of the flameholder. The illuminated particles in the combustor are imaged using a 12-bit MicroMAX Interline CCD camera (Roper-Scientific, 1300×1030 pixels) equipped with a 50 mm Nikkor lens ($f1/1.8$). The laser arrangement used in the PIV measurements is also shown in the schematic in Fig. 1. The particle displacements are obtained by dividing the PIV image into smaller interrogation windows for which a velocity vector is computed. The interrogation window size was 32×32 pixels, with a 50% overlap, which resulted in 31×39 vectors across the field, corresponding to a spatial size of 80 mm wide $\times$ 100 mm high. The delay between the laser pulses, 100 μs, was chosen such that 25% of the seeded particles remained in the interrogation window between two consecutive PIV images.

The temporal dynamics of the flame sheet were visualized by laser sheet scattering from olive oil (3–5 μm) seeded into the inlet air mixture. The oil droplets were generated using a Laskin nozzle design, with the nozzle immersed in the oil. The light sheet originates from an 8 W Coherent Innova 90 C continuous argon-ion laser of wavelength 514.3 nm. A cylindrical lens was used to provide a 4-mm-thick light sheet. At each operating condition, 8000 images were obtained without any spectral filtering at 1000 frames/s with an exposure time of 100 μs. The field of view is 89×89 mm, imaged at a resolution of 512 pixels horizontally and vertically. The images were captured by a high-speed intensified camera (Videoscope International, Ultracam3). The images, once captured, were then analyzed by tracking the high gradient contours that mark the flame edge. Raw laser sheet flame images (Fig. 2a) are first smoothed with a median filter and corrected for laser intensity variations; see Fig. 2b. The flame intensity gradients are then calculated at every point, as shown in Fig. 2c. The flame edge is associated with points at which this gradient exceeds 30% of the maximum value of the flame intensity gradient for a stable flame, as shown in Figs. 2d and 2e. This threshold level was selected by examining the probability density function of the intensity gradients of a stable flame. The extracted flame edge was overlaid with the raw image and found to closely conform to the visually deduced flame shape. Similarly, the flame edge was captured in the PIV images by the demarcation of the regions of high- and low-seeded flow.

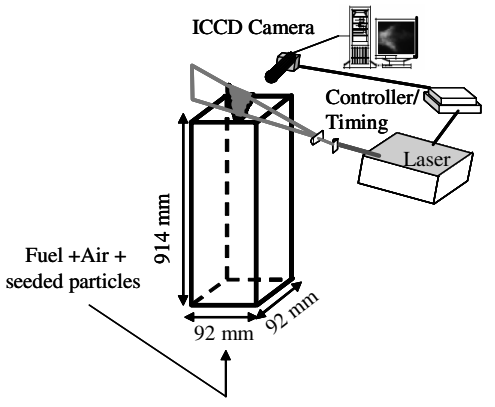

Fig. 1 Schematic of the bluff-body burner setup.

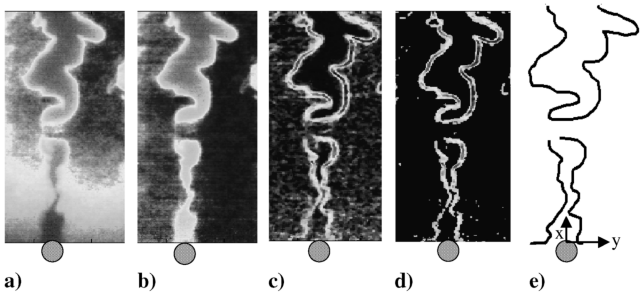

Fig. 2 Flame edge tracking: a) raw image, b) corrected image, c) image intensity gradients, d) thresholded image, and e) extracted flame edge. Flow direction is from bottom to top.

Acoustic oscillations were simultaneously measured using calibrated Bruel and Kjaer type 4939 condenser microphones. These have a flat frequency response up to 40 kHz and high sensitivity up to 4 mV/Pa. Their output was low-pass filtered at 2 kHz and then fed into a 12-bit, 16-channel National Instruments A/D board. A total of 65,536 (i.e., 2^{16} points) data points were obtained at a sampling frequency of 4.1 kHz. Acoustic emissions provide a useful diagnostic into transient flame holding events, because they are proportional to the temporal rate of change of the flame's global heat release (as opposed to the more localized optical diagnostics). The acoustic emissions of turbulent flames are dominated by unsteady heat release processes (as opposed to flow noise) [21–24] that excite acoustic waves over a broad range of frequencies.

III. Data Analysis Approaches

High-speed visualizations show the presence of flame wrinkles being generated near the flame holder and propagated in the mean flow direction. The amplitudes of these fluctuations vary with height and operating conditions. These flame images are postprocessed to determine the temporal location of the left and right flame branches as a function of height using the flame edge-tracking algorithm described previously. The coordinate system origin $(x, y) = (0, 0)$ point is the top of the bluff-body centerline, where x is the streamwise direction (downstream positive) and y is the transverse direction (right-side positive), as shown in Fig. 2e. Then, the flame location $L(x, t)$ is determined at each time instant t and spatial location x from the bluff body. The mean value of L at each x location is subtracted to obtain a flame front perturbation value $L'(\mathrm{x}, t) = L(x, t) - \langle L(x) \rangle$. The spectral content of the flame front position is determined with the Fourier transform to yield $L'(\mathrm{x}, f)$.

The 2-D flame stretch rate was quantified with the relations [25]:

$$\kappa = \kappa_s + \kappa_c$$

$$\kappa_s = -n_x \times n_y \times \left(\frac{\partial u}{\partial y} + \frac{\partial v}{\partial x}\right) + \left(1 - n_x^2\right) \times \frac{\partial u}{\partial x} + \left(1 - n_y^2\right) \times \frac{\partial v}{\partial y}$$

$$\kappa_c = S_L / R_c \qquad (2)$$

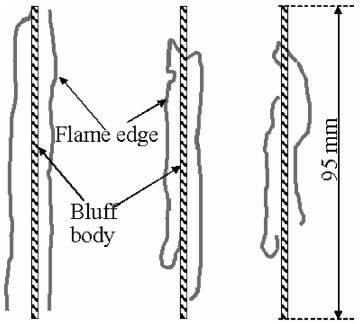

Fig. 3 Spanwise variation of the flame front corrugation for $\phi = 0.7$ (left), 0.63 (center), and 0.6 (right) at a height of 13 mm from the bluff body. Flow direction is normal to the plane of the paper, toward the reader.

The flame speed S_L was obtained from Andrews and Bradley [26]. The flame normals and curvatures were obtained from the flame edges and used in conjunction with the measured flowfield to determine the component of κ in the 2-D field of view.

It should be emphasized that three-dimensional effects, which cause the actual strain rate to differ from that calculated here, are not quantified in these calculations. Close to blowout, the flame does have some three-dimensional features, as can be seen by the cross stream visualization in Fig. 3, obtained by rotating the laser sheet by 90 deg, at a height of x = 13 mm from the bluff body. However, although these effects certainly will influence the quantitative results presented next, they do not change the qualitative trends. Furthermore, the flow and flame field, especially at the bluff-body centerline, are strongly two-dimensional (note that the three-dimensional effects are concentrated near the edges).

The uncertainties in the results are as follows: Based upon Monte Carlo simulations reported by Raffel et al. [27] the uncertainty in finding the peak cross-correlation location is estimated to be a maximum of 4 pixels. This includes the Gaussian subpixel interpolation error of 0.1 pixels that corresponds to 0.2% uncertainty in velocity component estimation. The interpolation error is determined by the grid size, the fluctuation of the velocity in the grid, and the velocity spatial gradient. The overall uncertainty in measuring each velocity component amounts to 8%. As detailed by Nair [28], the uncertainty in flame normal calculation varied from 4% for the case of a stable flame to 10% for the case close to blowout. Using standard propagation of error procedures, we estimate from Eq. (2) that these flame normal and velocity uncertainties lead to hydrodynamic flame stretch uncertainties κ_s, varying from 30% for a stable flame to 40% close to blowout. Using formulas obtained from Utcke [29] for estimating uncertainties in curvature of digitized images, we estimate the uncertainty in κ_s to be 5 and 20% at $\kappa_c = 100$ and 1000 1/s, respectively. The uncertainty is unbounded at $\kappa_c >$ 1700 1/s values, which coincides with the minimum resolvable radius of flame curvature. Note that these are uncertainties in the 2-D component of κ_c and κ_s; they do not account for uncertainties in their true value, due to the unresolved third dimension.

IV. Results

Tests were performed at atmospheric conditions at average and centerline velocities of 1.2 and 1.8 m/s in the absence of the bluff body at the channel exit, respectively. The latter velocity corresponds to a Reynolds number based on the bluff-body diameter of $Re_D =$ 640 and on channel width of $Re_W = 6200$. The approach flow was turbulent, with an intensity of 6% at the channel center. The mean velocity had a top-hat profile with a boundary-layer thickness of approximately 20 mm. The flame's proximity to blowout was controlled by decreasing the overall fuel flow rate while keeping the air flow rate fixed. The equivalence ratio was varied from 0.8 to its blowout value at 0.59.

A. Vorticity Dynamics

As will be shown later, the vorticity dynamics of the flow play an important role in its blowoff phenomenology. For this reason, we briefly summarize a few key points. In the absence of combustion and for the Reynolds number of interest, bluff-body flameholders naturally shed vortices. This asymmetric (about the bluff-body centerline) and coherent von Kármán vortex shedding occurs at a well-defined frequency $f \sim \beta U/D$ that scales with the bluff-body diameter D and the freestream flow velocity U [30]. The constant β typically has values on the order of 0.21, but does exhibit some Reynolds number and system geometry dependence. In the presence of combustion, however, the bluff-body near-field wake is characterized by a more symmetric flowfield dominated by shear-layer-induced vorticity that exhibits far less intense fluctuations and periodicity [14]. Although the full details of the physical mechanism behind the transition from the asymmetric von Kármán vortex solution of the nonreacting flow to a far less periodic solution in the presence of combustion are still being worked out, it is known that the altered vorticity dynamics of the bluff-body wake are critical [18,31].

For reference, the maximum cold-flow vorticity values are 400 s^{-1}. In the reacting case, a typical image of the flame and 2-D vorticity field for a well-stabilized flame is shown in Fig. 4, with solid and dashed lines indicating positive (counterclockwise) and negative (clockwise) vorticity, respectively. Note the irregularly spaced flame wrinkles that convect downstream. Note also that the vorticity field does not exhibit the spatially periodic distribution of alternately signed vorticity, evidenced in nonreacting flows. Vorticity is generated by the shear near the bluff body, as it is in the nonreacting flow. In addition, vorticity is generated by the baroclinic mechanism, given by $\nabla\rho x \nabla p/\rho^2$ in the vorticity transport equation, due to the misaligned gradients in pressure ∇p and density $\nabla\rho$, due to the inclination of the flame with respect to the flow. There is competition between baroclinic- and bluff-body-generated vorticity; these two sources are of the opposite sign. As such, the vorticity generated at the bluff body monotonically decays with downstream axial location by the action of baroclinic vorticity, so that the flow near and far from the bluff body is dominated by bluff-body- and baroclinic-generated vorticity, respectively [18]. This competition results in complete cancellation, and then sign reversal, of flow vorticity with downstream distance.

This competition has important implications upon the first stage of the flame's blowoff dynamics. As the equivalence ratio decreases, the magnitude of the flame-generated baroclinic vorticity source term decreases, due to the decreasing density jump across the flame. In addition, the vorticity damping term due to flow dilatation (given by $\boldsymbol{\omega}\nabla\cdot\boldsymbol{V}$ in the vorticity transport equation) also decreases. This necessarily means that *the flame near the bluff body experiences a higher magnitude vorticity field* than it did at higher equivalence ratios and a vorticity field that persists farther downstream. This is clearly seen in Figs. 5 and 6. Figure 5 plots the average vorticity field at two equivalence ratios, corresponding to a stable flame and one

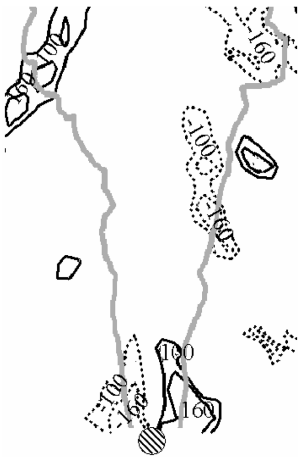

Fig. 4 Instantaneous vorticity contours (solid line, positive vorticity; dashed line, negative vorticity) along with flame front edge (gray solid line) of a stable flame at $\phi = 0.72$ (flow direction is from bottom to top).

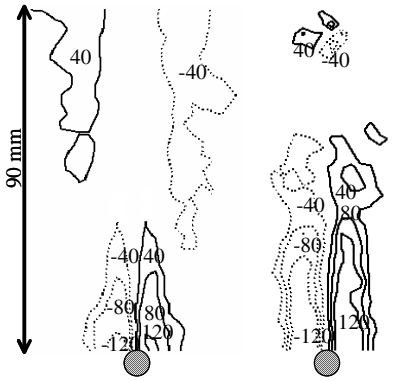

Fig. 5 Average vorticity contours (solid line, positive vorticity; dashed line, negative vorticity) of a stable flame (left) at $\phi = 0.72$ and of a flame close to blowout at $\phi = 0.63$ (right). Flow direction is from bottom to top.

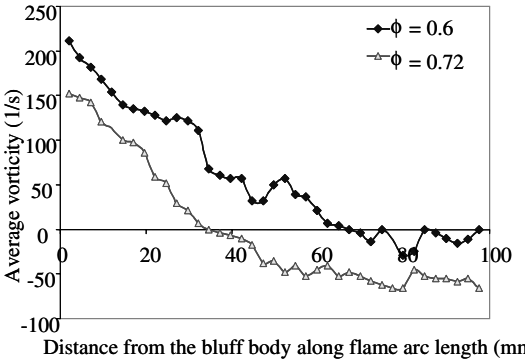

Fig. 6 Dependence of average vorticity as a function of distance from the bluff body along the flame arc length for $\phi = 0.72$ and 0.6.

close to blowout, averaged over 20 images. Note that the shear-generated vorticity effects have progressed further downstream as the equivalence ratio decreases, as expected. Note also the clear switch in sign of the average vorticity field, demarcating the shear and baroclinic-dominated near- and far-field regions. These features are clearly seen in Fig. 6, which plots the average vorticity as a function of distance from the bluff body along the flame arc length for $\phi = 0.72$ and 0.6. The average vorticity decreases with increasing axial distance for all cases and, at some point, switches sign from positive (bluff-body-generated vorticity) to negative (flame-generated vorticity). As the equivalence ratio is reduced, the effects of average bluff-body-generated vorticity have progressed further downstream.

B. Flame Stretch Effects

The flame near the bluff body has been shown to experience higher vorticity magnitudes as the equivalence ratio decreases. As such, the flame sees a higher fluid mechanic stretch κ_s [32]. Also, the larger amplitude vortical perturbations cause more significant perturbations on the flame front, increasing the magnitude of the curvature-induced stretch κ_c. These points will be quantified next. Furthermore, the flame is also more vulnerable to stretch, as its extinction stretch rate decreases with the equivalence ratio [33,34]. This section quantifies the flame stretch as blowout is approached. As will be shown, localized flame extinction by flame stretch is clearly present under near blowout characteristics.

The dependence of the extinction strain rates and actual strain rates experienced by the flame upon equivalence ratio are plotted in Fig. 7. The strain rate statistics quoted in this figure were obtained from 20 images at each ϕ value, using data obtained from a rectangular flow region two to four bluff-body diameters downstream (the number of spurious velocity vectors is much larger near the bluff body); given the fact that the vorticity magnitude decays with axial distance, the flame strain rate is certainly even higher close to the bluff body. Thus,

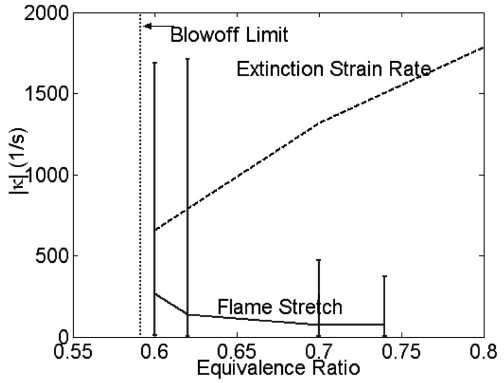

Fig. 7 Dependence of flame stretch rate (measured) and extinction stretch rate (calculated) upon equivalence ratio. Bars denote fluctuations in the flame stretch rates observed from 20 images.

these quoted measurements are based upon a total of 400 values. The extinction stretch rate was estimated using the OPPDIF program in CHEMKIN, using GRI 3.0 and assuming a methane/air flame at 298 K and 101.3 kPa reactants.

Before considering these data further, we should note two caveats to the data interpretation we will employ. First, the sensitivity of a flame to curvature and hydrodynamic-induced stretch is not necessarily the same at large stretch rates (although it is in the limit of weak stretch). As such, to be precise, note that the graph plots the extinction *hydrodynamic* strain rate κ_s. This use of κ_s seems reasonable, given that calculations and measurements indicate comparable κ_s and κ_c extinction strain rates for methane (but not in general) [35,36]. Second, the unsteady extinction strain rate is not necessarily the same as its steady state value (particularly because the dynamic response of a flame to hydrodynamic and curvature-induced stretch is quite different [37]). Nonetheless, the steady extinction strain rate provides insight into the stretch sensitivity of the flame and is a useful benchmark to compare the instantaneous values against.

Figure 7 is one of the key results of this work. It clearly illustrates the opposing trends of the instantaneous stretch rates that the flame sees and those that it is capable of withstanding before extinction. The vertical bars in the stretch rates do not signify uncertainty in the measurement, but rather the range in instantaneous values that the flame sees over the 20 images that were analyzed. Note the increasing magnitude of strain rate fluctuations with decreases in equivalence ratio, a point that will be discussed further, next. Furthermore, the actual strain rates at the two lowest equivalence ratios could be much higher; the maximum values shown in the plot are limited by camera resolution.

In comparison, the stretch rate for the cold-flow case was found to be substantially larger, $\sim$3000 s^{-1}, in the absence of combustion. Clearly, this value should only be interpreted for comparative purposes, as there is no flame in this case. This value was estimated from cold-flow velocity measurements at a spatial location coinciding with the average flame location. This comparison clearly shows the suppressed levels of vorticity in the reacting case due to gas expansion and baroclinic vorticity production.

Below some equivalence ratio, Fig. 7 shows that the local, instantaneous stretch rate exceeds the extinction stretch rate for certain instants of time, although not always. This is apparently the reason for the appearance of local points of extinction, "holes" in the flame that are observed to first occur below an equivalence ratio of $\phi = 0.65$; see Fig. 8. This sequence of consecutive images show the initiation of a hole, its convection downstream and impact upon the flame topology, and the reclosing of the flame hole. This phenomenon necessarily introduces some degree of unsteadiness in the flame, both in its position and in its total heat release.

These local flame extinction events, followed by flame recovery, are manifestations of the first of two stages in the unsteadiness experienced by near-blowoff flames. It should be emphasized that under such conditions, the flame can apparently persist indefinitely and is simply unsteady. Moreover, the overall position and

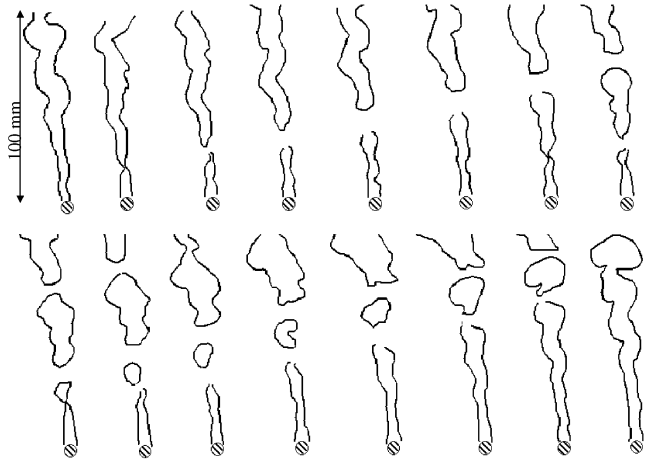

Fig. 8 Sequence of flame images, 10 ms apart, taken during the first preblowoff stage at $\phi = 0.65$. Note presence of flame holes in the images (flow direction is from bottom to top).

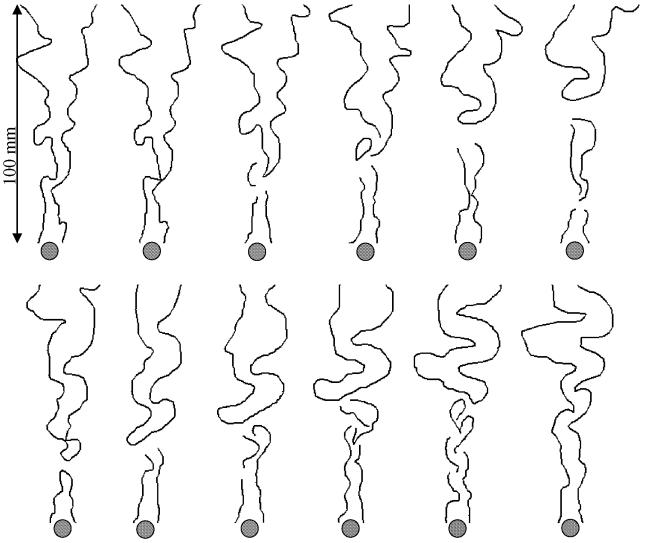

Fig. 9 Sequence of flame images, 6 ms apart, taken during the second preblowoff stage at $\phi = 0.6$ (flow direction is from bottom to top).

qualitative dynamics of the flame, in the instances for which it is continuous, appear essentially the same as that of the flame under stable conditions.

As the equivalence ratio is further decreased, the duration of these local flame extinction events increases monotonically. For example, the fraction of images with localized extinction events present increases from 0% at $\phi = 0.66$, to 8% at $\phi = 0.64$, to 40% at $\phi = 0.6$. The composition and temperature of the wake is locally altered with each occurrence of local flame extinction, as some portions of the wake no longer consist of simply hot recirculating products, but also cold reactants. As such, the average dilatation ratio between the cold reactants and cylinder wake must decrease faster than might be expected from a comparison of the temperature ratio between reactants and products.

Below an equivalence ratio of 0.62, there is large-scale alteration of the wake dynamics, as shown in Fig. 9. This is the second stage of the flame unsteadiness experienced before blowoff. As illustrated in the figures, the overall dynamics of the flowfield is clearly altered; in many cases, the flow in the bluff-body near field bears striking resemblance to the asymmetric von Kármán type flowfield. The strong stretching of the flame front is evident in these figures by, for example, the second to last image showing flame quenching inside what appears to be a series of consecutive flow structures. However, it should be emphasized that the flowfield and flame position are much more disorganized than that of cold-flow von Kármán vortex shedding. It reverts back and forth between synchronized, asymmetric wrinkles to what appears to be independent, asynchronous flame front distortions. Estimates from these images suggest that the time scales of these observed "structures" are of the order of 13–20 ms, corresponding to Strouhal number $Sr = 0.26$–0.39, using the centerline velocity of 1.8 m/s. These estimates were obtained by calculating the distance between subsequent structures in the flame images, shown in Fig. 9.

This second stage is also reflected in the acoustic emissions [21,22] from the flame, which are a measure of the unsteady flame heat release integrated over the entire flame zone. Figure 10 plots combustion noise spectra of the burner at two equivalence ratios, $\phi = 0.7$ and 0.6. As the equivalence ratio is reduced, the spectral component in the $Sr = 0.3$–0.5 range abruptly increases near blowout (using the centerline velocity of 1.8 m/s) and peaks at $Sr = 0.34$. Furthermore, spectral analysis of the fluctuation of the flame front $L'(x, f)$, plotted in Fig. 11, shows an abrupt growth of a peak in fluctuations at $Sr = 0.3$ as the equivalence ratio is reduced. Although these acoustic and flame position peak frequencies do not exactly coincide, such behavior can be expected due to the finite bandwidth of the two underlying signals. This can be seen as follows: assume that the flame position spectrum $L'(f)$ is proportional to the heat release $Q'(f)$. Because the sound emitted by heat release fluctuations $P'(f)$ scales as $P'(f) \sim fQ'(f)$ [38], the acoustic

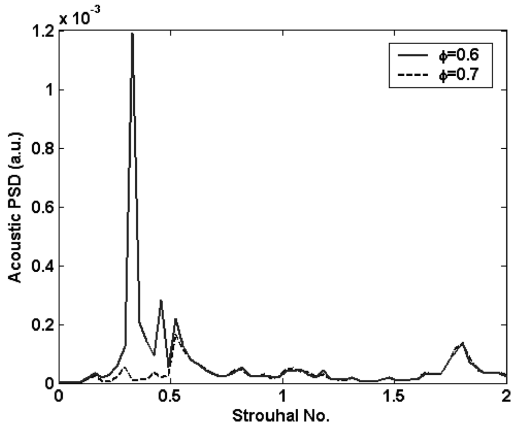

Fig. 10 Acoustic spectra from the bluff-body burner for $\phi = 0.7$ and 0.6.

emissions necessarily peaks at a slightly higher frequency than the heat release.

The initiation of this second stage has two consequences; first, it increases the overall unsteadiness of the flowfield. This is quantified in Fig. 7, which plots the large strain rate fluctuations at these low equivalence ratios. In addition, it is visually very obvious from the images, as the flame flaps back and forth violently. This second stage apparently coincides with the observations of Nicholson and Field [17] and the presence of flow periodicity deduced from LDV velocity measurements just before blowoff by Hertzberg et al. [14].

The second consequence of the initiation of this stage is that it increases the magnitude of the curvature contribution to the stretch term κ_c; see Eq. (2). For example, at $\phi = 0.7$, the maximum value of $|\kappa_c|$ was $\sim$470 s^{-1}, compared with the hydrodynamic stretch term $|\kappa_s| \sim 90$ s^{-1} in the region near the bluff body. In the second stage of blowout, this curvature term was dominant, due to the sharp kinks developed by the flame in the bluff-body near field, a result of the large-scale flame distortions. In this case, the value of $|\kappa_c|$ reached >1700 s^{-1} (the maximum resolvable value), compared with the hydrodynamic stretch term $|\kappa_s| \sim 160$ s^{-1}. In fact, extinction of the flame is plainly visible in these sharp kinks in some images.

V. Conclusions

Several questions raised by these results should be discussed. First, it is well known that the dynamics of nonreacting bluff-body flowfields vary with Reynolds number. As such, what is the

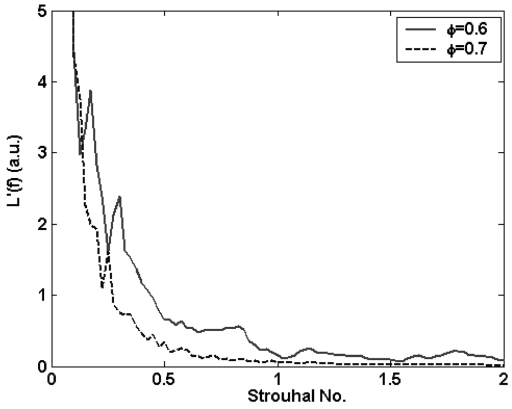

Fig. 11 Typical spectra of flame front fluctuations at a height of 75 mm from the bluff body at $\phi = 0.7$ and 0.6.

generality of these results to higher Reynolds numbers and other bluff-body configurations? The basic characteristics of the flow vorticity dynamics upon equivalence ratio noted in Fig. 6 are quite general. These trends can be deduced from basic consideration of vorticity transport; the fact that baroclinic vorticity is of opposite sign to that of the shear-generated vorticity should not change with Reynolds number or bluff-body configuration, assuming the pressure gradient remains similar. For example, recent measurements in an afterburner combustor simulator with a V-shaped flameholder at $Re_D \sim 20,000$ by Bush and Gutmark [39] show similar characteristics. Furthermore, the presence of localized flame extinction due to high strain rates is a fundamental combustion issue, which also should not be impacted by variations in Reynolds number.

The structure of the flow and organized vortical structures likely will change with Reynolds number, but in a manner that is unclear; for example, the presence and/or location of organized vortical structures in the near field of the bluff body under near-blowoff conditions. However, other results do suggest that similar flame dynamics appear at higher Reynolds numbers, as very similar images of the flame as seen in the second blowout stage reported here have been computed by Erickson et al. [19] at $Re = 45,000$.

A second issue is the relationship between the two preblowoff stages. In particular, is the presence of the first stage (i.e., localized flame extinction) a necessary condition for the second stage? The answer to this appears to be no, based upon simulation results of Erickson et al. [19], which solve a G equation for the flame position and do not include flame extinction and temporal flame liftoff. They clearly show the presence of large-scale flame corrugation and alteration of the bluff-body wake dynamics, results very similar to those reported here in Fig. 9. However, this behavior was only observed at very low dilatation ratio values, around $T_b/T_u = 1.5$. A common thread between these two results, however, may be the presence of a relatively small density ratio between the bluff-body wake and the unburned reactants. In our experiments, this was achieved through localized flame extinction, which results in cooling of the bluff-body wake by the recirculation of unburned reactants into it; even though the overall dilatation ratio between burned products and reactants has a value of 5–6. In the simulations of Erickson et al. [19], because there is no extinction, the altered wake dynamics occur at low dilatation ratios.

Finally, a word on the actual blowoff event. Figure 7 suggests that blowoff does not coincide with the point at which the average strain rate equals the extinction strain rate, as the flame blows off much earlier (however, it is possible that the inclusion of the third, unresolved dimension would alter this conclusion). As such, *blowoff must be precipitated by a time-localized extinction event* that is of large enough scale to cause irrecoverable blowoff. It is likely that initiation of this second stage is ultimately responsible for blowoff, as blowoff occurs at just a slightly lower equivalence ratio ($\phi = 0.59$) than the one at which this second stage initiates ($\phi \sim 0.62$). Perhaps one of the flame extinction events occurring in this second stage introduces a slug of unreacted mixture into the recirculation zone, which fails to ignite the incoming mixture, resulting in blowoff. This explanation can be seen to have some corollaries to the interpretation of Zukoski [12], according to which, flame extinction occurs when the fresh mixture does not spend enough time in the shear layer to be ignited by the hot recirculation zone. Although both interpretations ultimately consider a ratio of a chemical time and fluid mechanic time, Zukoski's interpretation stresses the ratio of their averages. In contrast, the present study emphasizes the instantaneous value of this ratio and the role of unsteady strain and fluid dynamics.

References

[1] Rosfjord, T. J., and Cohen, J. M., "Evaluation of the Transient Operation of Advanced Gas Turbine Combustors," *Journal of Propulsion and Power*, Vol. 11, No. 3, 1995, pp. 497–504.

[2] Schefer, R. W., Wicksall, D. W., and Agrawal, A. K., "Combustion of Hydrogen-Enriched Methane in a Lean Premixed Swirl-Stabilized Burner," *Proceedings of the Combustion Institute*, Vol. 29, Combustion Inst., Pittsburgh, PA, 2002, pp. 843–850.

[3] Shih, W. P., Lee, J., and Santavicca, D., "Stability and Emissions Characteristics of a Lean Premixed Gas Turbine Combustor," *Proceedings of the Combustion Institute*, Vol. 26, Combustion Inst., Pittsburgh, PA, 1996, pp. 2771–2778.

[4] Knaus, D. A., and Gouldin, F. C., "Measurements of Flamelet Orientations in Premixed Flames with Positive and Negative Markstein Numbers," *Proceedings of the Combustion Institute*, Vol. 28, Combustion Inst., Pittsburgh, PA, 2000, pp. 367–373.

[5] Chakravarthy, V. K., and Menon, S., "Large Eddy Simulations of Confined Bluff Body Stabilized Highly Turbulent Premixed Flames,"American Society of Mechanical Engineers Paper 99-7798, 1999.

[6] Rhee, C., Talbot, L., and Sethian, J., "Dynamic Behavior of Premixed Turbulent V-Flame," *Journal of Fluid Mechanics*, Vol. 300, Oct. 1995, pp. 87–115.

[7] Gouldin, F., and Cheng, R. K., "International Workshop on Premixed Turbulent Flames" *Premixed Turbulent Flames Database on CMCS* [online database], http://eetd.lbl.gov/aet/combustion/workshop/workshop.html [cited 16 Jan. 2006].

[8] Williams, G., Hottel, H., and Scurlock, A., "Flame Stabilization and Propagation in High Velocity Gas Streams," *Proceedings of the Combustion Institute*, Vol. 3, Combustion Inst., Pittsburgh, PA, 1951, pp. 21–40.

[9] Williams, G. C., and Shipman, C. W., "Some Properties of Rod Stabilized Flames of Homogeneous Gas Mixtures," *Proceedings of the Combustion Institute*, Vol. 4, Combustion Inst., Pittsburgh, PA, 1953, pp. 733–742.

[10] Longwell, J. P., Chenevey, J., Clark, W., and Frost, E., "Flame Stabilization by Baffles in a High Velocity Gas Stream," *Proceedings of the Combustion Institute*, Vol. 3, Combustion Inst., Pittsburgh, PA, 1951, pp. 40–44.

[11] Zukoski, E. E., "Afterburners," *Aero-Thermodynamics of Gas Turbine and Rocket Propulsion*, edited by G. Oates, AIAA, Reston, VA, 1997.

[12] Zukoski, E. E., and Marble, F. E., "The Role of Wake Transition in the Process of Flame Stabilization in the Bluff Bodies," *AGARD Combustion Researches and Reviews*, Butterworths, London, 1954, pp. 167–180.

[13] Cantwell, B., and Coles, D., "An Experimental Study of Entrainment and Transport in the Turbulent Near Wake of a Circular Cylinder," *Journal of Fluid Mechanics*, Vol. 136, Nov. 1983, pp. 321–374.

[14] Hertzberg, J. R., Shepherd, I. G., and Talbot, L., "Vortex Shedding Behind Rod Stabilized Flames," *Combustion and Flame*, Vol. 86, July 1991, pp. 1–11.

[15] Nair, S., "Acoustic Detection of Blowout Phenomenon," Ph.D. Thesis, Georgia Inst. of Technology, Atlanta, May 2006.

[16] Nair, S., and Lieuwen, T., "Acoustic Detection of Blowout in Premixed Flames," *Journal of Propulsion and Power*, Vol. 21, 2005, pp. 32–39.

[17] Nicholson, H., and Field, J., "Some Experimental Techniques for the Investigation of the Mechanism of Flame Stabilization in the Wake of Bluff Bodies," *Proceedings of the Combustion Institute*, Vol. 3, Combustion Inst., Pittsburgh, PA, 1951, pp. 44–68.

[18] Soteriou, M. C., and Mehta, P. G., "Combustion Heat Release Effects on the Dynamics of Bluff Body Stabilized Premixed Reacting Flows," AIAA Paper 2003-0835, 2003.

[19] Erickson, R., Soteriou, M., and Mehta, P., "The Influence of Temperature Ratio on the Dynamics of Bluff Body Stabilized Flames," AIAA Paper 2006-0753, 2006.

[20] Westerweel, J., "Fundamentals of Digital Particle Image Velocimetry," *Measurement Science and Technology*, Vol. 8, No. 12, 1997, pp. 1379–1392.

[21] Hurle, I. R., Price, R. B., Sugden, T. M., and Thomas, A., "Sound Emission from Open Turbulent Premixed Flames," *Proceedings of the Royal Society of London*, Series A, Vol. 303, 1968, pp. 409–427.
[22] Katsuki, M., Mizutani, Y., Chikami, M., and Kittaka, T., "Sound Emission from a Turbulent Flame," *Proceedings of the Combustion Institute*, Vol. 21, Combustion Inst., Pittsburgh, PA, 1986, pp. 1543–1550.
[23] Kotake, S., and Takamoto, K., "Combustion Noise: Effects of the Velocity Turbulence of Unburned Mixture," *Journal of Sound and Vibration*, Vol. 139, May 1990, pp. 9–20.
[24] Putnam, A. A., "Combustion Roar of Seven Industrial Burners," *Journal of the Institute of Fuel*, Vol. 49, Sept. 1976, pp. 135–138.
[25] Chung, S. H., and Law, C. K., "An Invariant Derivation of Flame Stretch," *Combustion and Flame*, Vol. 55, Aug. 1984, pp. 123–125.
[26] Andrews, G. E., and Bradley, D., "Burning Velocity Of Methane-Air Mixtures," *Combustion and Flame*, Vol. 19, Oct. 1972, pp. 275–288.
[27] Raffel, M., Willert, C., and Kompenhans, J., *Particle Image Velocimetry: A Practical Guide*, Springer–Verlag, Berlin, 1998.
[28] Nair, S., "Acoustic Characterization of Flame Blowout Phenomenon," Ph.D. Thesis, Georgia Inst. of Technology, Atlanta, 2006.
[29] Utcke, S., "Error Bounds on Curvature Estimation," in *Scale-Space 2003*, edited by L. D. Griffin, and M. Lillholm, Springer–Verlag, Heidelberg, Germany, 2003, pp. 657–666.
[30] Williamson, C. H. K., "Vortex Dynamics in the Cylinder Wake," *Annual Review of Fluid Mechanics*, Vol. 28, Jan. 1996, pp. 477–539.
[31] Coats, C. M., "Coherent Structure in Combustion," *Progress in Energy and Combustion Science*, Vol. 22, No. 5, 1996, pp. 427–509.
[32] Rehm, J. E., and Clemens, N. T., "Relationship Between Vorticity/Strain and Reaction Zone Structure in Turbulent Non-Premixed Jet Flames," *Proceedings of the Combustion Institute*, Vol. 27, Combustion Inst., Pittsburgh, PA, 1998, pp. 1113–1120.
[33] Poinsot, T., and Veynante, D., *Theoretical and Numerical Combustion*, R. T. Edwards, Flourtown, PA, 2001.
[34] Sung, C. J., and Law, C. K., "Extinction Mechanisms of Near-Limit Premixed Flames and Extended Limits of Flammability," *Proceedings of the Combustion Institute*, Vol. 26, Combustion Inst., Pittsburgh, PA, 1996, pp. 865–873.
[35] Kobayashi, H., and Kitano, M., "Extinction Characteristics of a Stretched Cylindrical Premixed Flame," *Combustion and Flame*, Vol. 76, Nos. 3–4, 1989, pp. 285–296.
[36] Wang, P., Hu, S., Wehrmeyer, J., and Pitz, R., "Stretch and Curvature Effects on Flames," AIAA Paper 2004-148, 2004.
[37] Joulin, G., "On the Response of Premixed Flames to Time Dependent Stretch and Curvature," *Combustion Science and Technology*, Vol. 97, Apr. 1994, pp. 219–229.
[38] Strahle, W. C., "On Combustion Generated Noise," *Journal of Fluid Mechanics*, Vol. 49, No. 2, 1971, pp. 399–414.
[39] Bush, S., and Gutmark, E., "Reacting and Nonreacting Flow Fields of a V-Gutter Stabilized Flame," AIAA Paper 2006-807, 2006.

J. Oefelein
Associate Editor